The First Radio Spectrum of a Rapidly Rotating A-type Star

Jacob Aaron White[1,14] ⓘ, F. Tapia-Vázquez[2,3] ⓘ, A. G. Hughes[4] ⓘ, A. Moór[5,6], B. Matthews[7] ⓘ, D. Wilner[8] ⓘ, J. Aufdenberg[9], O. Fehér[10] ⓘ, A. M. Hughes[11] ⓘ, V. De la Luz[3,12] ⓘ, A. McNaughton[9,13] ⓘ, and L. A. Zapata[2] ⓘ

[1] National Radio Astronomy Observatory, 520 Edgemont Road, Charlottesville, VA 22903, USA; jwhite@nrao.edu
[2] Instituto de Radioastronomía y Astrofísica, Universidad Nacional Autónoma de México, P.O. Box 3-72, 58090, Morelia, Michoacán, México
[3] GICC, Interdisciplinary Group of Scientific Computing, UNAM, México
[4] Department of Physics and Astronomy, University of British Columbia, 6224 Agricultural Road, Vancouver, BC V6T 1T7, Canada
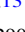[5] Konkoly Observatory, Research Centre for Astronomy and Earth Sciences, Eötvös Loránd Research Network (ELKH), Konkoly-Thege Miklós út 15-17, 1121 Budapest, Hungary
[6] ELTE Eötvös Loránd University, Institute of Physics, Pázmány Péter sétány 1/A, 1117 Budapest, Hungary
[7] Herzberg Institute, National Research Council of Canada, 5071 W. Saanich Road, Victoria, BC V9E 2E7, Canada
[8] Center for Astrophysics, Harvard & Smithsonian, 60 Garden Street, Cambridge, MA 02138, USA
[9] Physical Sciences Department, Embry-Riddle Aeronautical University, 600 S Clyde Morris Boulevard, Daytona Beach, FL 32114, USA
[10] IRAM, 300 Rue de la piscine, F-38406 Saint-Martin-d'Hères, France
[11] Department of Astronomy, Van Vleck Observatory, Wesleyan University, 96 Foss Hill Drive, Middletown, CT 06459, USA
[12] Escuela Nacional de Estudios Superiores Unidad Morelia, Universidad Nacional Autònoma de México, Morelia, 58190, México
[13] Earth & Biological Sciences Directorate, Biological Sciences Division, Pacific Northwest National Laboratory, Richland, WA 99352, USA

Abstract

The radio spectra of main-sequence stars remain largely unconstrained due to the lack of observational data to inform stellar atmosphere models. As such, the dominant emission mechanisms at long wavelengths, how they vary with spectral type, and how much they contribute to the expected brightness at a given radio wavelength are still relatively unknown for most spectral types. We present radio continuum observations of Altair, a rapidly rotating A-type star. We observed Altair with NOEMA in 2018 and 2019 at 1.34, 2.09, and 3.22 mm and with the Very Large Array in 2019 at 6.7 and 9.1 mm. In the radio spectra, we see a brightness temperature minimum at millimeter wavelengths followed by a steep rise to temperatures larger than the optical photosphere, behavior that is unexpected for A-type stars. We use these data to produce the first submillimeter to centimeter spectrum of a rapidly rotating A-type star informed by observations. We generated both PHOENIX and KINICH-PAKAL model atmospheres and determine the KINICH-PAKAL model better reproduces Altair's radio spectrum. The synthetic spectrum shows a millimeter brightness temperature minimum followed by significant emission over that of the photosphere at centimeter wavelengths. Together, these data and models show how the radio spectrum of an A-type star can reveal the presence of a chromosphere, likely induced by rapid rotation, and that a Rayleigh Jean's extrapolation of the stellar photosphere is not an adequate representation of a star's radio spectrum.

Unified Astronomy Thesaurus concepts: Radio continuum emission (1340); Stellar atmospheres (1584); Circumstellar matter (241); Submillimeter astronomy (1647); Millimeter astronomy (1061)

1. Introduction

The internal structure of main-sequence stars, and thus the mechanism(s) for generating magnetic fields, is largely dependent on mass and therefore spectral type (Charbonneau 2013). M-type stars can be fully convective and generate strong magnetic fields through an α^2 dynamo (e.g., Chabrier & Küker 2006). K- through early F-type stars have radiative cores with convective outer layers, and the shear between these zones is thought to play a critical role in magnetic field generation (e.g., Guerrero et al. 2016). A-type and more massive stars are mostly radiative and unable to generate strong magnetic fields. Shorlin et al. (2002) confirm through a spectropolarimetric survey that main-sequence "normal" A-type stars do not have significant magnetic fields. Some A-type stars, however, and in particular those that are chemically peculiar, have been observed to have nonnegligible magnetic field strengths (see, e.g., Preston 1974).

Stellar magnetic fields and convective zones can heat the upper atmosphere and are therefore associated with chromospheric and coronal activity (Ayres 2010). For these stars, the radio emission is proportional to the plasma temperature (T_R) in the atmosphere and is dominated by optically thick free–free radiation from electrons, ions, and H^- (Liseau et al. 2013; Linsky 2017). Therefore, a brightness temperature (T_B) spectrum can trace the temperature and density structure. Radio observations with broad spectral coverage provide a reliable method of measuring the thermal emission as a function of height above the stellar surface and modeling the thermal structure of the atmosphere (e.g., the KINICH-PAKAL (KP) modeling code Tapia-Vázquez & De la Luz 2020). Higher atmospheric temperatures in the chromosphere can lead to a higher T_B at radio wavelengths, and are evidenced by a rise in the spectrum at wavelengths >1 mm (Loukitcheva et al. 2004; White et al. 2020).

For solar-like stars, the submillimeter (submm) emission is expected to arise from the photosphere (Liseau et al. 2013). At ∼millimeter wavelengths, the emission is generated in both the upper photosphere and lower chromosphere. At millimeter–centimeter wavelengths, the emission is expected to arise from the lower to the upper chromosphere (Liseau et al. 2016). At >centimeter wavelengths, the emission comes from the upper chromosphere and lower corona (Trigilio et al. 2018).

A-type stars lack significant stellar convectivity, meaning chromosphere and corona are not expected. This in principle

---

leads to a thermal submillimeter–centimeter spectrum largely representative of the optical photosphere in the Rayleigh–Jeans limit. For Sirius A, a slowly rotating A0V star, radio observations (White et al. 2018a, 2019) and PHOENIX photosphere models (Hauschildt & Baron 1999) show a spectrum slightly cooler than the photosphere and no evidence of an increase in T_B that could be attributed to a chromosphere or corona (for details on PHOENIX and KINICH-PAKAL modeling codes, see Section 3.2).

In general, stellar spectra in the submillimeter–centimeter wavelength regime are difficult to accurately model due to the lack of empirical data in this portion of the spectrum that can be used to inform existing models. The dominant atmospheric processes and structure that determine the spectral shape rely strongly on intrinsic stellar properties. While a model of a single spectral type may be applicable to a few stars, it may significantly over- or underpredict the flux of many other stars, depending on the wavelength.

In this Letter, we present the first submillimeter to centimeter spectrum and model of Altair (α Aql, HD 187642). This 1.3 Gyr A7IV-V star is one of the most studied objects in our solar neighborhood (5.13 ± 0.01 pc; van Leeuwen 2007). Altair is known for low amplitude pulsation (δ Scuti classification; Buzasi et al. 2005), rapid rotation ($v \sin(i) = 190$–250 km s^{-1}; Abt & Morrell 1995), and significant oblateness (e.g., Monnier et al. 2007; CHARA measures a polar radius of 1.63 $R_\odot$ and an equatorial radius of 2.03 $R_\odot$). This oblateness has contributed to a 6860–8450 K temperature gradient from the equator to the poles (surface averaged temperature of 7594 K; Bouchaud et al. 2020), although it is unclear if this temperature gradient is present at longer wavelengths. Altair's rapid rotation has created a stable equatorial dynamo, which generates stronger than expected magnetic fields for an A-type star (Robrade & Schmitt 2009). In addition, UV spectroscopy shows evidence of significant heating in Altair's upper atmosphere (Walter et al. 1995), which is interpreted by some as chromospheric emission (Simon et al. 1995). This hotter upper atmosphere may cause significant deviations from an assumed thermal spectrum at long wavelengths as well.

These results are part of The MESAS Project (Measuring the Emission of Stellar Atmospheres at Submillimeter/centimeter wavelengths), an ongoing observational campaign that seeks to build a catalog of radio spectra of main-sequence stars. This project uses long wavelength data to inform stellar atmosphere modeling codes in order to better understand the dominant stellar emission mechanisms at these wavelengths.

2. Observations

The analysis in this Letter uses new observations and archival data from Herschel and the Very Large Array Sky Survey (VLASS). The observations and calibration procedures for the NOrthern Extended Millimeter Array (NOEMA) and NSF's Karl G. Jansky Very Large Array (VLA) data are described in the Appendix. The primary observational results are summarized in Table 1.

Figure 1 shows Altair's radio spectrum. This spectrum clearly deviates from a blackbody (black line) at multiple wavelengths and such a model will over- or underpredict the flux depending on the wavelength. On the right side of Figure 1, we show Altair's spectrum as a fraction of the photosphere temperature. We calculate the brightness

temperature assuming an elliptical emitting area using the polar and equatorial radii. In this spectral representation, 1.0 indicates an observed radio T_B equal to the surface averaged optical photosphere temperature of 7594 K. This figure allows for a straightforward comparison of different spectral types. In addition to Altair models, Figure 1 includes a KP model of γ Vir A (White et al. 2020), a quiet Sun model (Loukitcheva et al. 2004), and a PHOENIX model of Sirius A (White et al. 2018a, 2019). The PHOENIX and KP models are detailed in Section 3.2.

3. Discussion

Data-informed atmosphere models of solar-like stars, such as the Sun and γ Vir A, have a shallow T_B minimum below 1 mm and a large increase in T_B at wavelengths over 1 mm. This increase is due to the presence of a stellar chromosphere and corona, which contribute to significant emission over the photosphere (Loukitcheva et al. 2004; White et al. 2020). Altair appears to exhibit a very strong T_B minimum, dropping to at least $0.2 \times T_{\rm phot}$. The representative wavelength of the minimum is unknown due to a lack of 0.25–1.29 mm data. Regardless, from 1.29 to 3.48 mm the T_B rapidly rises back to near the photosphere temperature ($\sim 0.80 \times T_{\rm phot}$). At longer wavelengths, the rise continues.

As Altair is an A7V star, and data-informed atmosphere models of A-type stars are largely nonexistent in the literature, it may have been naively assumed that Altair's radio spectrum would be similar to that of Sirius A (an A0V star; included in Figure 1). Altair's spectrum, however, significantly deviates from a Sirius-like profile. Since Altair is rapidly rotating, leading to an equatorial magnetic dynamo, the possibility exists that its spectrum would be more similar to magnetically active stars such as the Sun with significant emission in the chromosphere (e.g., Ayres 2010). Comparing Altair's spectrum to a quiet Sun model (e.g., the orange line on the right-hand-side of Figure 1; Loukitcheva et al. 2004) we see that a solar-like model may be more representative than a Sirius-like model, but still does not adequately explain the spectrum.

3.1. Spectral Index

A given stellar emission mechanism will have a characteristic spectral index, α, related to the observed flux by $F_\lambda \propto \lambda^\alpha$. Therefore, a spectral index can be a powerful diagnostic tool for disentangling emission mechanisms and can provide information about the structure of a star's atmosphere. Thermal emission from an optically thick source will have a spectral index of $\alpha = -2$. Given a lack of observational data at long wavelengths, this values of α is commonly assumed to be the representative for A-type stars in the Rayleigh–Jeans limit and is used to, e.g., estimate the stellar flux contribution in circumstellar disk studies (see Section 3.3). Since Altair's spectrum is clearly not well represented by a blackbody model, then there are likely additional emission/absorption mechanisms contributing to its spectrum.

In Figure 2, we show Altair's spectrum along with spectral indices fit to subsets of the data using a least squares approach with the SciPy function *curve_fit* (Virtanen et al. 2020). For $\lambda < 1.98$ mm, we calculate a spectral index of $\alpha_{\rm submm} = -2.10 \pm 0.04$. Within the 1σ uncertainties, this is consistent with a deviation from the thermal photospheric emission in the Rayleigh–Jeans regime. A similar cooler

Table 1
Summary of the New Observations Presented Here and Data from the Literature

Wavelength (mm)	Facility	Date YYYY MMM DD	Flux Calibrator	Beam Size ($''$)	Beam PA ($°$)	Flux Density (μJy)	Uncertainty (μJy)
0.10	Herschel[a]	2010 May 9	⋯	⋯	⋯	329020	18880
0.16	Herschel[a]	2010 May 9	⋯	⋯	⋯	148260	9940
0.25	Herschel[b]	2011 Nov 16	⋯	⋯	⋯	55700	8300
1.29	NOEMA	2018 May 17	MWC349[c]	$2.''68 \times 1.''60$	10.5	431	107
1.38	NOEMA	2018 May 17	MWC349	$2.''85 \times 1.''68$	5.9	548	83.9
1.98	NOEMA	2018 May 12	MWC349	$3.''44 \times 2.''11$	6.9	705	45.0
2.20	NOEMA	2018 May 12	MWC349	$3.''82 \times 2.''27$	7.5	668	32.8
2.96	NOEMA	2018 Apr 28	MWC349	$2.''78 \times 1.''64$	31.5	384	25.1
3.48	NOEMA	2018 Apr 28	MWC349	$3.''18 \times 1.''85$	40.0	283	29.8
1.29	NOEMA	2019 Feb 7	MWC349	$0.''76 \times 0.''37$	28.4	395	75.1
1.38	NOEMA	2019 Feb 7	MWC349	$0.''79 \times 0.''39$	28.9	342	66.0
1.98	NOEMA	2019 Feb 8	MWC349	$1.''14 \times 0.''53$	17.2	596	45.6
2.20	NOEMA	2019 Feb 8	MWC349	$1.''18 \times 0.''58$	18.7	469	36.7
2.96	NOEMA	2019 Feb 15	MWC349	$1.''64 \times 0.''75$	17.2	286	30.8
3.48	NOEMA	2019 Feb 15	MWC349	$1.''84 \times 0.''86$	18.0	262	27.7
6.7	VLA	2019 Mar 15, 19, 24	3C 48[d]	$0.''22 \times 0.''17$	−32.4	83	21.9
9.1	VLA	2019 Mar 15, 19, 24	3C 48[d]	$0.''25 \times 0.''21$	−21.6	57	5.9
100	VLASS[e]	2017 Oct 25	⋯	$2.''68 \times 2.''32$	25.5	<120[f]	⋯

Notes. The NOEMA and VLA data use a best-fit flux from modeling the visibility data as described in Appendices A.1 and A.2, respectively. The $\sigma_{\rm rms}$ uncertainties are from the CLEANed images and do not include an absolute flux calibration uncertainty. The calibration uncertainties are ∼20% at 1 mm and 10% at 3 mm for NOEMA, and ∼20% at 6.7 mm and ∼15% at 9.1 mm for the VLA.
[a] Herschel PACS photometry data (Thureau et al. 2014).
[b] Photometry data from the Herschel SPIRE Point Source Catalog (Schulz et al. 2017).
[c] The flux calibrator MWC349 for NOEMA was observed in each of the tracks and its model flux was used to derive the flux of the calibrators and the source.
[d] The quasar 3C 48, which was used to calibrate the flux from the VLA observations, has been undergoing a flare since early 2018 and therefore contributes to a larger absolute flux calibration uncertainty than is typical for these wavelength data (see Appendix A.2).
[e] VLASS data obtained the CIRADA server.
[f] Altair was not detected in the VLASS data; therefore the $\sigma_{\rm rms}$ of the area around Altair's expected location is taken as an upper level limit to the flux.

spectrum with a slightly steeper spectral index was observed in Sirius A and is well-reproduced by a PHOENIX atmosphere model (black line in Figure 1; White et al. 2018a, 2019). We do not include the 1.3 mm data in the spectral index calculations as the drop in T_B to 1000–2000 K is not reconcilable with any known physical mechanism (see Section 3.2).

For wavelengths in the range of 1.98 mm $< \lambda < 10$ mm, the spectral index has a value of $\alpha_{\rm mm} = -1.59 \pm 0.10$. In this portion of the spectrum, the spectral index is in broad agreement with solar-like stars (e.g., Villadsen et al. 2014; Liseau et al. 2016), where chromospheric emission begins to contribute significantly to the observed flux. Considering only the VLA data, we find $\alpha_{\rm cm} = -1.21 \pm 0.17$, continuing the trend toward higher brightness temperatures and a possible contribution from chromospheric emission. Due to the lack of data at wavelengths longer than 1 cm we are unable to determine if the centimeter spectral index is also solar-like.

### 3.2. Stellar Atmosphere Models

To model Altair's spectrum, we consider both PHOENIX (Hauschildt & Baron 1999) and KP atmospheres (Tapia-Vázquez & De la Luz 2020). The PHOENIX model includes only the stellar photosphere whereas the KP model includes chromospheric emission from above the photosphere. The MESAS Project previously used PHOENIX to model Sirius A (White et al. 2018a, 2019) and KP to model γ Lep, γ Vir A, and γ Vir B (White et al. 2020).

The PHOENIX approach (version 17.01.02A) includes a gravity-darkened model for Altair's photosphere. We adopted Altair's "β-fixed" parameters (Monnier et al. 2007) and a

$0.''19495$ parallax (van Leeuwen 2007). We used the modeling code from Aufdenberg et al. (2006), which was previously used to model the photosphere of the rapid-rotator Vega (a similar approach is also used in Lipatov & Brandt 2020). We used 1D PHOENIX model atmospheres to generate 117 LTE radiation fields evaluated at 78 different angles, $T_{\rm eff}$ values from 6750 to 8750 K in 250 K intervals, and $\log_{10}(g)$ values from 3.90 to 4.40 in 0.05 intervals. The temperature–pressure structure of each model atmosphere in radiative equilibrium was computed assuming a hydrostatic atmosphere, including between 1719584 and 1842901 spectral lines in LTE, depending on $T_{\rm eff}$ and $\log_{10}(g)$ values, and 576 bound–bound and bound–free transitions from hydrogen and helium in non-LTE. We then sampled the oblate surface with 100 latitude points and 300 longitude points, integrating the intensities to produce a synthetic photosphere spectrum (see Figure 1).

KP is a nonlinear framework that computes a stellar atmosphere spectrum through a 1D NLTE semiempirical model of the chromosphere at long wavelengths. KP uses PakalMPI (De la Luz et al. 2011) to generate an atmosphere structure in hydrostatic equilibrium and to compute a synthetic spectrum taking into account three opacity functions (Bremsstrahlung, H^-, and inverse Bremsstrahlung). A Levenberg–Marquardt algorithm is used to iteratively modify the T_R profile, fitting the synthetic spectrum to the observed radio fluxes. KP computed 11848 atmospheres to obtain a new semiempirical model of the Altair. The last radial T_R profile is then smoothed using a Savitzky–Golay filter with a seventh-order polynomial. This model is equilibrated again with
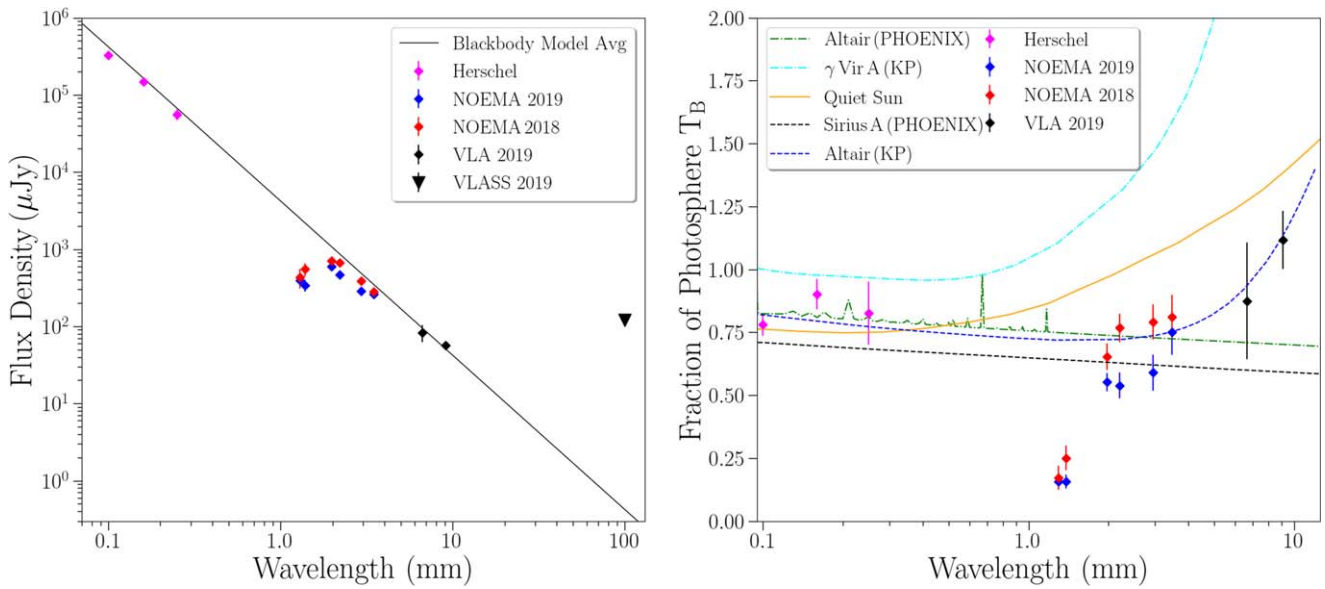
Figure 1. Left: Altair's spectrum. The data from Table 1 are plotted along with the VLASS $\sigma_{\rm rms}$ from the nondetection at 100 mm (3 GHz) included for illustrative purposes. The solid black line is a 7594 K blackbody model and is included to show the significant deviations at different wavelengths. Right: Altair's fractional T_B spectrum and different stellar emission models. The y-axis is T_B divided by the optical photosphere temperature (where 1.0 represents pure blackbody emission). The cyan line is a KP model (Tapia-Vázquez & De la Luz 2020) of the F0IV star γ Vir A (White et al. 2020). The orange line is a quiet Sun model (Loukitcheva et al. 2004). The black line is a PHOENIX model (Hauschildt & Baron 1999) of the A0V star Sirius A (White et al. 2018a, 2019). The blue and green lines are KP and PHOENIX models of Altair (see Section 3.2). The PHOENIX and KP models are detailed in Section 3.2.
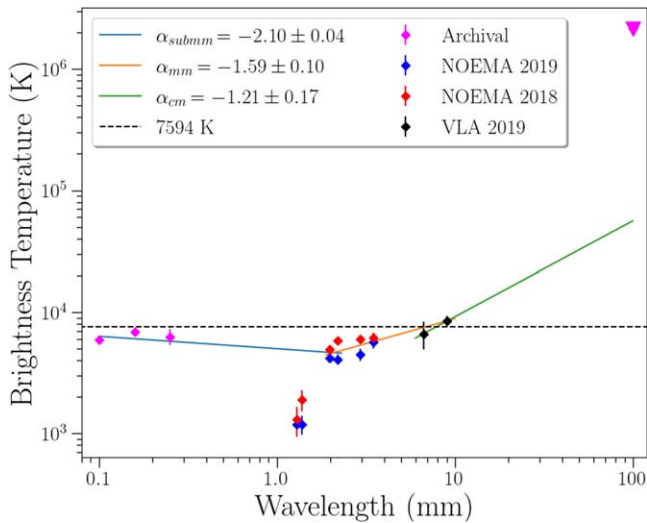
Figure 2. Altair's T_B spectrum. The Herschel data are plotted in purple, the VLA data are in black, and the 2018 and 2019 NOEMA data are in red and blue, respectively. The $\sigma_{\rm rms}$ of the VLASS nondetection is denoted by the upside down triangle. The 7594 K average optical photosphere temperature (black line) represents a spectral index of $\alpha = -2.0$. The submillimeter spectral index (blue line) is $\alpha_{\rm submm} = -2.10 \pm 0.04$. This fit is to only the Herschel and NOEMA 2 mm data. The millimeter spectral index (orange line) is $\alpha_{mm} = -1.59 \pm 0.10$. This fits from the NOEMA 2 mm data to the VLA 9 mm data. The cm spectral index (green line) is $\alpha_{cm} = -1.21 \pm 0.17$ and only fits the VLA data.

PakalMPI to guarantee the hydrostatic equilibrium. The final model structure is shown in Figures 3(a)–(b).

We determine that the KP model better reproduces the data and include the final semiempirical model in Figure 3. This model shows that for wavelengths <1 mm the emission comes from the photosphere and for >3 mm the emission originates in the chromosphere. This is due to an optically thick atmosphere at altitudes where T_R is below 10,000 K and is not fully ionized.

At 2083 km above the photosphere, we find a T_R minimum of 4207 K ($T_{R,\rm min}/T_{\rm eff} \approx 0.55$) and a hydrogen density of $n_{\rm H} = 1.5 \times 10^{11}\,{\rm cm}^{-3}$. Overall, T_R gradually decreases until reaching a minimum, typical of photospheric behavior. Starting at a height of 2083 km, we observe a positive temperature gradient that extends for $\sim$100 km. T_R then plateaus at 10,000 K and extends $\sim$200 km further. At this point, T_R gradually rises, similar to the chromospheric behavior in models obtained by Gouttebroze et al. (1999) and Ferrero et al. (1995). In Figure 3(c) we plot the contribution function (CF; Tapia-Vázquez & De la Luz 2020) to constrain where the emission is generated.

Previous modeling approaches primarily considered Altair's UV spectrum to compute the structure of the upper photosphere and chromosphere. Anomalies in the C II line were speculated to be from ISM absorption (Gouttebroze et al. 1999). Our model could not produce the observed 1.3 mm T_B minimum and therefore we did not include these data in the final KP or PHOENIX results. If there is significant foreground absorption, it is not clear if this feature is observable at 1.3 mm. Absorption from interstellar grains would yield a broad feature with a spectral index reflective of the grain's size distribution (e.g., Jones et al. 1996). At 1.3 mm, Altair's emission would be predominantly absorbed by $\sim$millimeter-sized grains, and ISM grains are typically a few micrometers in size (e.g., Weingartner & Draine 2001). If the absorption is from a molecular line, e.g., CO(2–1) with a rest frequency of 230.53 GHz (1.3 mm), then the approximately flat spectral index between the NOEMA sidebands of 1.29 and 1.38 mm implies a line width $\geqslant 0.1$ mm and a velocity of $\sim 10^4\,{\rm km\,s}^{-1}$, which is unphysical for the ISM. We determine that the 1.3 mm data are likely not contaminated by foreground material.

The observed 1.3 mm flux density is broadly consistent between the two NOEMA semesters. After consultation with NOEMA support scientists we conclude that significant instrument or calibration uncertainties are unlikely. While
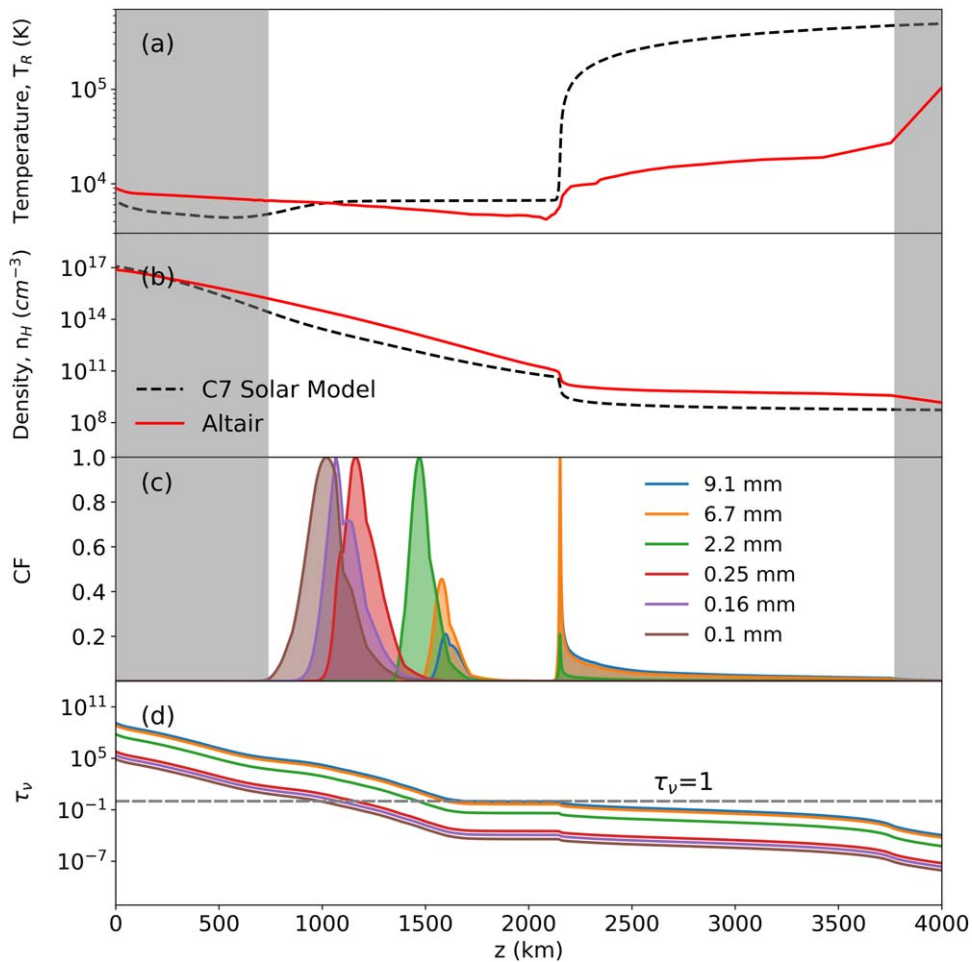
Figure 3. KP model of Altair's atmosphere as a function of height above the photosphere ($z = 0$ at $\tau_{500\,nm} = 1$). The shaded regions represent the outer boundaries where KP cannot be accurately applied. (a) The red line shows Altair's T_R profile. The black line is the C7 solar model (Avrett & Loeser 2008) used as initial conditions. (b) Density profile of Altair (red line) and the average solar values (black line). (c) Normalized contribution function (CF) for Altair. At 9.1 mm, the maximum contribution occurs at 2152 km and a second peak at 1596 km has a contribution of 21%. At 6.7 mm, the CF has a maximum at 2152 km and a second peak at 1578 km with a contribution of 45%. At 2.2 mm, the maximum is reached at 1470 km and a second peak at 2152 km with a contribution of 21%. At 0.25 mm, 0.16 mm, and 0.10 mm, the CF shows peaks at 1162 km, 1065 km, and 1019 km, respectively. (d) The optical depth at each wavelength.

there is no known physical mechanism that could reproduce the 1.3 mm flux, we cannot rule out an anomalous absorption or opacity in Altair's atmosphere without more data. Future observations at 0.25–1.3 mm, and follow-up observations at 1.3 mm with another facility such as ALMA, are therefore imperative to accurately determine the cause of the observed drop in flux.

3.3. Applicability to Observations of Debris Disks

The radio spectra obtained with The MESAS Project are useful outside the context of stellar atmospheric processes. Historically, the presence of debris disks are inferred by excess over the expected stellar emission at a given wavelength when the disks cannot be spatially resolved (Aumann et al. 1984). The first star observed in the campaign was Sirius A, a star with no known circumstellar debris (White et al. 2018a). Radio observations of Sirius A were used to inform a PHOENIX model atmosphere. This spectrum was applied to the millimeter emission of Fomalhaut, an A3V star very similar to Sirius A but with an extended debris disk (e.g., Kalas et al. 2005; Acke et al. 2012; White et al. 2017). In addition to Fomalhaut's well-resolved debris ring, there is an inferred inner asteroid belt that has not been resolved (Acke et al. 2012). Such an asteroid belt

would be collisionally evolving to produce millimeter-sized debris that may be detectable at millimeter wavelengths. Instead, Fomalhaut's millimeter emission has a spectrum nearly identical to that of Sirius A (Su et al. 2016; White et al. 2017), which has no known debris. This result casts doubt on the presence of an additional debris component in the Fomalhaut system (White 2018) and highlights the importance of an accurate radio stellar spectrum to determine the presence and characteristic of unresolved circumstellar debris.

3.4. Future Work

As is clear from Altair's observed radio spectrum, determining the stellar flux at a given wavelength based solely on the flux at a different wavelength is nontrivial. In order to fully characterize the radio spectrum of Altair, observations between 0.25 and 1.29 mm are imperative. The only facility that can fill in the gap on Altair's missing data is ALMA. Follow-up observations at all wavelengths with multiple cadences will assess the long-term variability or stability of Altair's radio emission.

The MESAS Project is currently pushing state-of-the-art radio observatories to their limits. Proposed future facilities, such as the next generation Very Large Array (ngVLA), will be

invaluable for revealing stellar atmosphere structures. For example, the ngVLA will yield a 93 GHz (3.22 mm) continuum $\sigma_{rms} = 0.40\text{--}1.0\,\mu$Jy beam^{-1} in 1 hr[15] In addition, a majority of the proposed ngVLA antennas will have a maximum baseline of 1000 km, giving a resolution of 0.66 mas. The ngVLA will resolve Altair by 5–6 beam widths in only a few minutes of integration time. This level of detail is absolutely imperative to determine how the high rotational velocity, and resulting dynamo, can impact the overall T_B structure of the star. The ngVLA's unprecedented sensitivity means all G-type and brighter stars are detectable within $\sim$75 pc, allowing for a comprehensive survey of our solar neighborhood (see, e.g., Carilli et al. 2018; White et al. 2018b).

4. Conclusions

We present the first observationally informed submillimeter to centimeter spectrum of a rapidly rotating A-type star. We observed Altair with NOEMA and VLA at 1.29–9.1 mm in 2018 and 2019. The data were used to inform both PHOENIX and KINICH-PAKAL stellar atmosphere modeling codes. We conclude that the KINICH-PAKAL model better reproduces the data. This temperature spectrum is cooler than the photosphere at $<$1 mm then becomes much hotter at $>$3 mm, indicative of a chromosphere. The radio spectrum deviates from that expected for both A-type stars and cooler F/G-type stars. In addition, the significantly smaller flux observed at 1.3 mm may be due to an anomalous opacity that we were unable to reproduce in our models. These results are part of The MESAS Project, an ongoing observational campaign that seeks to build a radio catalog of main-sequence stars.

Appendix
Observational Data

A.1. NOEMA

Altair was observed with NOEMA in 2018 April 28, 12, and May 17 (ID W17BF, PI White), and in 2019 February, 7, 8,

and 15 (ID W18BQ, PI White). The observations were centered on Altair using J2000 coordinates R.A. $= 19^h50^m46\overset{s}{.}996$ and $\delta = +08°52'05\overset{''}{.}956$ and accounting for proper motion. The observations in 2018 used nine antennas in the C and D configurations with baselines ranging from 24–293 m and 24–176 m, respectively. The observations in 2019 used 10 antennas in the A configuration with baselines ranging from 32 to 760 m.

The observations used the Band 1, Band 2, and Band 3 instruments with the PolyFiX correlator and 4064×2 MHz channels in each band. In Band 1, the rest frequency of each baseband was tuned to 214.208, 218.269, 229.693, and 233.754 GHz. In Band 2, they were tuned to 134.215, 138.276, 149.700, and 153.761 GHz. In Band 3, they were tuned to 84.219, 88.280, 99.704, and 103.766 GHz. An identical instrument setup was used in 2018 and 2019. The data calibration pipeline and imaging utilized the GILDAS software packages and was done with the assistance of NOEMA contact scientists at IRAM. In 2018, quasars J2002 +150 and 1932+204 were used for phase and amplitude calibration and MWC349 was used to calibrate the absolute flux. The Band 1 and Band 2 observations used 3C 345 for bandpass calibration and 3C 454.3 was used for Band 3. In 2019, all bands used quasars J2002+150 and J1938+048 for phase and amplitude calibrations and MWC349 for absolute flux calibration. Quasars 1633+382, 1749+096, and 3C 345 were used as bandpass calibrators in Band 1, Band 2, and Band 3, respectively.

In each of the three receivers, the two upper sidebands were combined and the two lower sidebands were combined to increase the signal-to-noise. This gives effective wavelengths of 1.29, 1.38, 1.98, 2.20, 2.96, and 3.48 mm for each data point. To derive the flux at each wavelength, we used the GILDAS MAPPING package and the *UVFIT* task to fit a point-source model directly to the visibilities (see Table 1 for a list of fluxes). We used the *UVMAP* task to make dirty image maps and then Hogbom cleaning to a threshold of one-half the rms noise. The σ_{rms} of the images is adopted as the representative uncertainty for each data point. The absolute flux calibration uncertainty for NOEMA is $\sim$20% at 1 mm and less than 10% at 3 mm.[16]

In 2018, from shortest to longest wavelength, the observations achieve sensitivities and synthesized beams of 107 μJy beam^{-1} and $2\overset{''}{.}68 \times 1\overset{''}{.}60$ at a position angle (PA) of $10\overset{°}{.}5$; 83.9 μJy beam^{-1} and $2\overset{''}{.}85 \times 1\overset{''}{.}68$ at a PA of $5\overset{°}{.}9$; 45.0 μJy beam^{-1} and $3\overset{''}{.}44 \times 2\overset{''}{.}11$ at a PA of $6\overset{°}{.}9$; 32.8 μJy beam^{-1} and $3\overset{''}{.}82 \times 2\overset{''}{.}27$ at a PA of $7\overset{°}{.}5$; 25.1 μJy beam^{-1} and $2\overset{''}{.}78 \times 1\overset{''}{.}64$ at a PA of $31\overset{°}{.}5$; and 29.8 μJy beam^{-1} and $3\overset{''}{.}18 \times 1\overset{''}{.}85$ at a PA of $40\overset{°}{.}0$, respectively.

In 2019, the observations achieve sensitivities and synthesized beams of 75.1 μJy beam^{-1} and $0\overset{''}{.}76 \times 0\overset{''}{.}37$ at a PA of $28\overset{°}{.}4$; 66.0 μJy beam^{-1} and $0\overset{''}{.}79 \times 0\overset{''}{.}39$ at a PA of $28\overset{°}{.}9$; 45.6 μJy beam^{-1} and $1\overset{''}{.}14 \times 0\overset{''}{.}53$ at a PA of $17\overset{°}{.}2$; 36.7 μJy beam^{-1} and $1\overset{''}{.}18 \times 0\overset{''}{.}58$ at a PA of $18\overset{°}{.}7$; 30.8 μJy beam^{-1} and $1\overset{''}{.}64 \times 0\overset{''}{.}75$ at a PA of $17\overset{°}{.}2$; and 27.7 μJy beam^{-1} and $1\overset{''}{.}84 \times 0\overset{''}{.}86$ at a PA of $18\overset{°}{.}0$, respectively.

---

[15] For estimated ngVLA sensitivities, see http://library.nrao.edu/public/ memos/ngvla/NGVLA_21.pdf.

[16] NOEMA absolute flux calibration uncertainties https://www.iram.fr/ IRAMFR/GILDAS/doc/html/pdbi-cookbook-html/pdbi-cookbook.html.

A.2. VLA

The data from the VLA were acquired during three Scheduling Blocks (SBs) on 2019 March 15, 19, and 24 (ID 19A-141, PI White). The observations were centered on Altair using J2000 coordinates R.A. $= 19^h50^m46\overset{s}{.}996$ and $\delta = +08°52'05\overset{''}{.}956$ and accounted for proper motion. The data used 27 antennas in the B configuration with baselines ranging from 0.21 to 11.1 km.

Each SB used an identical instrument configuration and observing strategy. The 33 GHz data utilized the *Ka*-band tuning setup with 4×2.048 GHz basebands and rest frequency centers of 28.976, 31.024, 34.976, and 37.024 GHz, yielding an effective frequency of 33 GHz (9.1 mm). The 45 GHz data utilized the *Q*-band tuning setup with 4×2.048 GHz basebands and rest frequency centers of 41.024, 43.072, 46.968, and 48.976 GHz, yielding an effective frequency of 45 GHz (6.7 mm).

The SBs were reduced using the CASA 5.4.0 pipeline (McMullin et al. 2007), which included bandpass, flux, and phase calibrations. For all SBs, quasar J1950+0807 was used for phase and bandpass calibrations. Quasar 0137+331 = 3C 48 was used as a flux calibration source for all SBs. 3C 48 was originally intended to also be used as a bandpass calibrator, but the ongoing flare and a low signal-to-noise in each SPW made it unreliable. Upon consultation with the VLA HelpDesk, we modified the scan intents of the raw data to identify J1950 +0807 as the bandpass calibrator and proceeded with a standard pipeline calibration. The ongoing flare of the calibrator increased absolute flux uncertainty to ∼20% in the *Q* band and ∼15% in the *Ka* band.[17]

The three SBs were concatenated using the CASA task *concat*. To derive the flux at each wavelength, we used the CASA task *uvmodelfit* to fit a point-source model at each frequency. The concatenated data were imaged with a natural weighting and cleaned using CASA's *CLEAN* algorithm down to a threshold of one-half the rms noise. The observations achieve a sensitivity of 21.9 μJy beam^{-1} and 5.9 μJy beam^{-1} for the 6.7 mm and 9.0 mm data, respectively. The size of the resulting synthesized beam is $0\overset{''}{.}22 \times 0\overset{''}{.}17$ at a position angle of $-32\overset{°}{.}4$ and $0\overset{''}{.}25 \times 0\overset{''}{.}21$ at a position angle of $-21\overset{°}{.}6$, respectively.
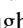
A.3. Literature Data

In addition to the new data presented here, we also include Herschel and VLA Sky Survey (VLASS) data from the literature in our analysis. Altair was observed with the Herschel PACS instrument at 0.10 mm and 0.16 mm on 2010 May 9. We use the two IR photometry data points of Altair presented in Thureau et al. (2014) as part of the DEBRIS survey (we note that the authors report no excess flux that could be attributed to circumstellar material). The observed flux was 329.02 ± 18.88 mJy and 148.26 ± 9.94 mJy at 0.10 mm and 0.16 mm, respectively. We also use Herschel SPIRE data from the Herschel Point Source Catalog (Schulz et al. 2017). Altair was observed with SPIRE on 2011 November 16. The observed flux was 55.7 ± 8.3 mJy at 0.25 mm.

VLASS is an all-sky survey with uniform sensitivity at 3 GHz (100 mm) covering three separate epochs. At the time of writing, only one epoch had been completed. We downloaded a

1′ section of the sky centered on the J2000 coordinates of Altair from The Canadian Initiative for Radio Astronomy Data Analysis (CIRADA) server.[18] The observations were made on 2017 October 25 and have a synthesized beam size of $2\overset{''}{.}68 \times 2\overset{''}{.}32$ and a position angle of $25\overset{°}{.}5$. Altair was not detected, but we use the $\sigma_{\rm rms} = 120\ \mu$Jy beam^{-1} from the surrounding area as an upper level limit on the 3 GHz flux.

ORCID iDs

Jacob Aaron White ● https://orcid.org/0000-0001-8445-0444
F. Tapia-Vázquez ● https://orcid.org/0000-0001-9132-7196
A. G. Hughes ● https://orcid.org/0000-0002-3446-0289
B. Matthews ● https://orcid.org/0000-0003-3017-9577
D. Wilner ● https://orcid.org/0000-0003-1526-7587
O. Fehér ● https://orcid.org/0000-0003-3453-4775
A. M. Hughes ● https://orcid.org/0000-0002-4803-6200
V. De la Luz ● https://orcid.org/0000-0003-0257-4158
A. McNaughton ● https://orcid.org/0000-0002-4146-7921
L. A. Zapata ● https://orcid.org/0000-0003-2343-7937

References

Abt, H. A., & Morrell, N. I. 1995, ApJS, 99, 135
Acke, B., Min, M., Dominik, C., et al. 2012, A&A, 540, A125
Aufdenberg, J. P., Mérand, A., Du Foresto, V. C., et al. 2006, ApJ, 645, 664
Aumann, H. H., Gillett, F. C., Beichman, C. A., et al. 1984, ApJL, 278, L23
Avrett, E. H., & Loeser, R. 2008, ApJS, 175, 229
Ayres, T. 2010, MmSAI, 81, 553
Bouchaud, K., de Souza, A. D., Rieutord, M., et al. 2020, A&A, 633, A78
Buzasi, D. L., Bruntt, H., Bedding, T. R., et al. 2005, ApJ, 619, 1072
Carilli, C. L., Butler, B., Golap, K., et al. 2018, in ASP Conf. Ser. 517, Science with a Next Generation Very Large Array, ed. E. Murphy (San Francisco, CA: ASP), 369
Chabrier, G., & Küker, M. 2006, A&A, 446, 1027
Charbonneau, P. 2013, in Solar and Stellar Dynamos, ed. O. Steiner (Berlin: Springer), 187
De la Luz, V., Lara, A., & Raulin, J.-P. 2011, ApJ, 737, 1
Ferrero, R. F., Gouttebroze, P., Catalano, S., et al. 1995, ApJ, 439, 1011
Gouttebroze, P., Ferrero, R. F., Marilli, E., et al. 1999, A&A, 348, 198
Guerrero, G., Smolarkiewicz, P. K., Dal Pino, E. D. G., et al. 2016, ApJ, 819, 104
Hauschildt, P. H., & Baron, E. 1999, JCoAM, 109, 41
Jones, A. P., Tielens, A. G. G. M., & Hollenbach, D. J. 1996, ApJ, 469, 740
Kalas, P., Graham, J. R., & Clampin, M. 2005, Natur, 435, 1067
Linsky, J. L. 2017, ARA&A, 55, 15
Lipatov, M., & Brandt, T. D. 2020, ApJ, 901, 100
Liseau, R., De la Luz, V., O'Gorman, E., et al. 2016, A&A, 594, A109
Liseau, R., Montesinos, B., Olofsson, G., et al. 2013, A&A, 549, L7
Loukitcheva, M., Solanki, S. K., Carlsson, M., et al. 2004, A&A, 419, 747
McMullin, J. P., Waters, B., Schiebel, D., et al. 2007, in ASP Conf. Ser. 376, Astronomical Data Analysis Software and Systems XVI, ed. R. A. Shaw, F. Hill, & D. J. Bell (San Francisco, CA: ASP), 127
Monnier, J. D., Zhao, M., Pedretti, E., et al. 2007, Sci, 317, 342
Preston, G. W. 1974, ARA&A, 12, 257
Robrade, J., & Schmitt, J. H. M. M. 2009, A&A, 497, 511
Schulz, B., Marton, G., Valtchanov, I., et al. 2017, SPIRE Point Source Catalog Explanatory Supplement, arXiv:1706.00448
Shorlin, S. L. S., Wade, G. A., Donati, J. F., et al. 2002, A&A, 392, 637
Simon, T., Drake, S. A., & Kim, P. D. 1995, ASP, 107, 1034
Su, K. Y., Rieke, G. H., Defrére, D., et al. 2016, ApJ, 818, 45
Tapia-Vázquez, F., & De la Luz, V. 2020, ApJS, 246, 5
Thureau, N. D., Greaves, J. S., Matthews, B. C., et al. 2014, MNRAS, 445, 2558
Trigilio, C., Umana, G., Cavallaro, F., et al. 2018, MNRAS, 481, 217
van Leeuwen, F. 2007, A&A, 474, 653
Villadsen, J., Hallinan, G., Bourke, S., et al. 2014, ApJ, 788, 112
Virtanen, P., Gommers, R., Oliphant, T. E., et al. 2020, NatMe, 17, 261
Walter, F. M., Matthews, L. D., & Linsky, J. L. 1995, ApJ, 447, 353
Weingartner, J. C., & Draine, B. T. 2001, ApJ, 548, 296

---

[17] For a note on the VLA flux calibration uncertainty, see science.nrao.edu/facilities/vla/docs/manuals/oss/performance/fdscale.

[18] CIRADA cutout service at URL cutouts.cirada.ca.

White, J. A. 2018, PhD Thesis, Univ. British Columbia https://doi.org/10.
    14288/1.0368801
White, J. A., Aufdenberg, J., Boley, A. C., et al. 2018a, ApJ, 859, 102
White, J. A., Aufdenberg, J., Boley, A. C., et al. 2018b, in ASP Conf. Ser. 517,
    Science with a Next Generation Very Large Array, ed. E. Murphy (San
    Francisco, CA: ASP), 171

White, J. A., Aufdenberg, J., Boley, A. C., et al. 2019, ApJ, 875, 55
White, J. A., Boley, A. C., Dent, W. R. F., et al. 2017, MNRAS, 466, 4201
White, J. A., Tapia-Vázquez, F., Hughes, A. G., et al. 2020, ApJ, 894, 76